REAL-TIME SIMULATION OF ROTOR INFLOW USING A COUPLED FLIGHT DYNAMICS AND FLUID DYNAMICS SIMULATION

J. Bludau * J. Rauleder † L. Friedmann ‡ M. Hajek §
Institute of Helicopter Technology
Technical University of Munich, 80333 Munich, Germany

In order to predict the rotorcraft motion in the vicinity of objects or their wake, a real-time capable model is presented. The dynamic inflow into the rotors was extracted from a real-time Lattice-Boltzmann fluid simulation and fed into a blade element based rotorcraft flight dynamics code. To represent the influence of arbitrary objects on the flight dynamics, the objects were modeled by boundary conditions in the Lattice-Boltzmann fluid simulation and updated dynamically in every time step. This two-way coupled simulation enabled the prediction of the rotorcraft motion and flight dynamics in arbitrary situations without prior knowledge of the flow field. To validate the effect of objects on the inflow, the required power in hover and forward flight in ground effect was evaluated. Furthermore, the rotorcraft motion due to a step input in hovering and forward flight was discussed. The results from the coupled fluid dynamics/flight dynamics model showed good agreement when compared to a more established reference model, namely the Pitt-Peters inflow model.

Nomenclature

A_{cell}	Area of projection of the cell onto the rotor disk, m^2
A_{int}	Area of polygon resulting from intersection, m^2
BEM	Blade element method
c_s	Smagorinksy constant
$\boldsymbol{cos}_l$	Vector of cosine coefficients of lth order, N
d	Cell length in fluid solver, m
$\Delta\Psi$	Halve angle of circular segment, rad
$\boldsymbol{f}$	Vector of volume force in cell, N
$\boldsymbol{f}_{\boldsymbol{perCell}}$	Vector of volume force per cell inside the rotor, N
LBM	Lattice-Boltzmann method
N	Cells per edgelength of cubic domain in the fluid solver
N_b	Number of blades
N_{harm}	Number of included harmonics
N_{in}	Number of cells fully within the rotor
N_ψ	Number of points in circumferential direction
N_R	Number of blade elements
$North, East, Down$	Positions of rotorcraft center of gravity in North-East-Down system, m
p_{cg}, q_{cg}, r_{cg}	Rotation rates of rotorcraft center of gravity in cg system, deg/s
P_{IGE}	Power in ground effect, kW
P_{OGE}	Power out of ground effect, kW

* Graduate Student, jakob.bludau@tum.de
† Assistant Professor, juergen.rauleder@tum.de
‡ Former Research Assistant, friedmann@tum.de
§ Professor and Department Head, hajek@tum.de

©2016

Φ, Θ, Ψ	Attitudes of rotorcraft center of gravity in North-East-Down system, deg
r	Radial blade coordinate, m
R	Main rotor radius, m
$RANS$	Reynolds-averaged Navier–Stokes
$\boldsymbol{sin}_l$	Vector of sine coefficients of lth order, N
t	Time, s
$\boldsymbol{T}_i$	Thrustvector of blade i, N
$\boldsymbol{u}$	Vector of inflow velocities, m/s
u_{cg}, v_{cg}, w_{cg}	Velocities of rotorcraft center of gravity in cg system, m/s
x_{cg}, y_{cg}, z_{cg}	Coordinates in the body-fixed coordinate system in the center of gravity
$x_{lbm}, y_{lbm}, z_{lbm}$	Coordinates in the fluid solver coordinate system
z	Height above ground, m

1 INTRODUCTION

Rotorcraft flight in the vicinity of large objects or in non-uniform and non-stationary flow conditions of the surrounding air are among the most challenging situations for pilots. As the objects and wakes influence the rotors, the reaction of the rotorcraft to pilot inputs is altered. This requires the pilot to adapt to the constantly changing flight dynamics while being in high-workload situations. A well known example is the take-off and landing on moving ship decks at quickly changing wind speeds and directions. In order to be able to train pilots to master such situations safely and without risk for man and machine, it is inevitable to provide training in flight simulators. Therefore, a real-time capable simulation of rotorcraft flight dynamics that captures the influence of arbitrary surroundings and flow environments on the flight behavior and handling qualities is necessary.

As the forces of the rotors mainly define the rotorcraft's dynamics, the correct calculation of the aerodynamic forces produced by the rotors is of particular importance. Therefore, the local angle of attack along the blades and the velocity relative to the air is necessary. The resulting lift and drag cause the blades to perform lead-lag and flapping motions, which change the local angle of attack and therefore the resulting aerodynamic forces. Furthermore, the aerodynamic forces accelerate the air when passing through the rotor, inducing a very complex inflow into the rotors. This inflow changes the local angle of attack of the blades. In order to capture the correct rotor dynamics, the angle of attack, blade motion, and forces inside the rotor are needed, which depend strongly on the inflow of air. Therefore, the inflow is modeled as a function of the aerodynamic forces. In this regard one widely used model is the Pitt-Peters dynamic inflow model [1] which was used as the reference model in the current work.

There are various approaches to enhance models like the Pitt-Peters model which assume uniform flow conditions upstream of the rotors and the absence of objects in the rotor wake. One example is the model of Gennaretti et al. [2] who used higher-order coefficients to account for the non-uniformity of the inflow. Nevertheless, these models are not capable of representing the influence of arbitrary objects surrounding the rotorcraft. Other approaches use RANS based computational fluid dynamics to calculate the flow field, which enables them to capture the influence of nearby objects [3–6]. Unfortunately, the computational costs eliminate the real-time capability. Thus, databases with external flow field data have to be created as a preliminary step. In a similar manner, experimental data of the flow field can be used although, this limits the validity to reviously measured cases, geometries and flow conditions. Another recently developed approach used the free vortex wake method on graphic cards in order to achieve real-time capability [7].

In contrast, the presented method used a modified version of the comparably low-resolution fluid dynamics solver which was developed in-house at the Technical University of Munich [8]. This solver was coupled with a blade element based flight dynamics code (BEM) to calculate the rotorcraft motion in arbitrary flight situations using arbitrary boundary conditions. As the influence of objects and wakes is transported to the rotors by the fluid simulation, the resulting effects on the rotorcraft motion can be captured by the BEM code. The resulting thrust was imposed as a volume force in the flow simulation. This two-way coupling enabled the model to capture the dynamic influence of the surroundings of the rotorcraft on its flight dynamics and on the produced flow field in real-time; an example is shown in Fig. 1.

©2016

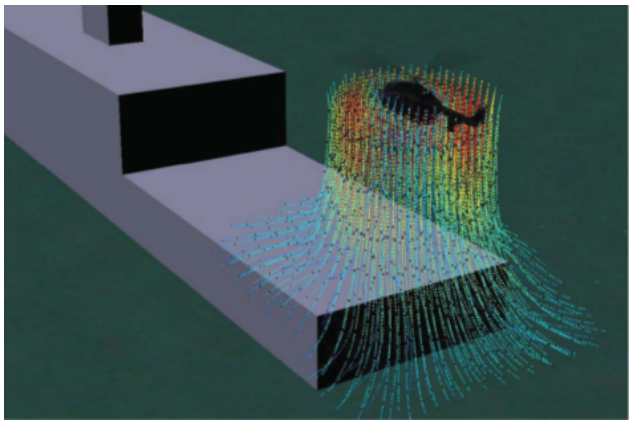

Figure 1: **Visualization of the flow field around the Bo 105 helicopter hovering above a ship deck. Colored streamlines used to indicate direction and velocity of the flow.**

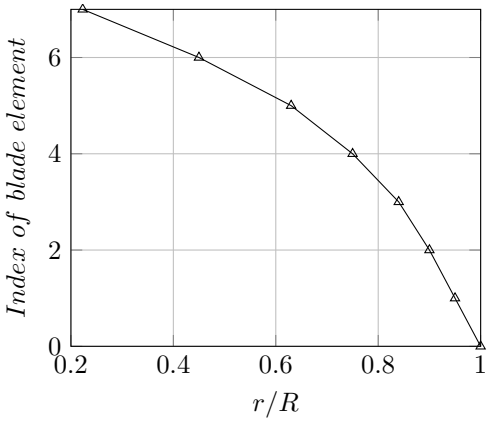

Figure 2: **Radial position of the blade elements used in the BEM code.**

2 MODELING APPROACH

2.1 Simulation of rotorcaft dynamics

Throughout this paper, the considered rotorcraft was a MBB Bo 105 helicopter with a total mass of $2500\,kg$ and a main rotor radius of $R = 4.92\,m$. The used BEM code modeled the main rotor as being fully articulated, allowing lead-lag, flap and feathering motion. The blades were modeled as rigid. In radial direction each blade was discretized with $N_R = 8$ blade elements. These were placed from $\frac{r}{R} = 0.223$ up to $\frac{r}{R} = 1$ in decreasing distances towards the blade tip, as can be seen in Fig. 2. The section of $\frac{r}{R} < 0.223$ was assumed to be aerodynamically neutral and therefore producing neither thrust nor drag. This assumption is valid, because the velocity resulting from the rotation of the blades dominates the absolute velocity of the blade element relative to the air. As this circumferential speed at $\frac{r}{R} < 0.223$ is low compared to the speed at the outer sections of the blade, and the blade not having an aerodynamic profile, the resulting lift and drag of this section of the blade are comparably small and they were therefore neglected for simplicity.

In circumferential direction $N_\Psi = 72$ positions for the azimuth Ψ were used. The forces on the blade at these positions were calculated by interpolating lift and drag from profile polars at the blade elements and integrating over the blade length using the Simpson rule. The aerodynamic forces of the fuselage and empennage were interpolated from polars similar to the forces of the blades.

As the rotors were represented by actuator disks in the fluid simulation, the thrust at every radial and circumferential position inside the disk was needed. In order to provide this, the BEM code turned the rotor until the blade motion and forces were steady over the revolution of the rotor. By this, the forces of the blades were no longer dependent on the position and velocity of the blade at the beginning of the timestep, and the thrust that had to be imposed on the actuator disk was extracted. At low frequency inputs or variations in the inflow into the rotors, this assumption is valid as the blade motion adjust after about one revolution, which is very fast compared to the reaction of the rotorcraft [9]. Unfortunately, this steady state assumption alters the rotor dynamic behavior at frequencies in the range of the rotor's rotational frequency, as the blades do not reach stationary motion and forces per revolution. Nevertheless, it is shown in Sec. 3.2 that for the imposed step inputs in combination with an actuator disk to represent the rotors, the steady state assumption is valid.

2.2 Numerical setup of the fluid solver

The used fluid dynamics solver is based on the Lattice-Boltzmann method (LBM). Therefore, the Boltzmann equation is approximated using discrete cells containing particle distributions and a collision operator to account for particle interactions which results in a weakly compressible fluid behavior [10, 11]. For details on the solver see Ref. [8]. It was embedded in a framework which dynamically generated boundary conditions in order to represent nearby obstacles [8]. This enabled the real-time calculation of the flow field even when the rotorcraft or the objects were in motion.

The fluid domain in the LBM solver was cubic with an edge length of $4R$ with R being the main rotor radius. Inside this domain the main rotor was located one R from the top. This left $3R$ below the rotor to capture the ground effect which becomes negligible at heights larger than $3R$ above ground [12]. A schematic view of the domain and grid is depicted in Fig. 3.

The resolution N of the simulation was defined

©2016

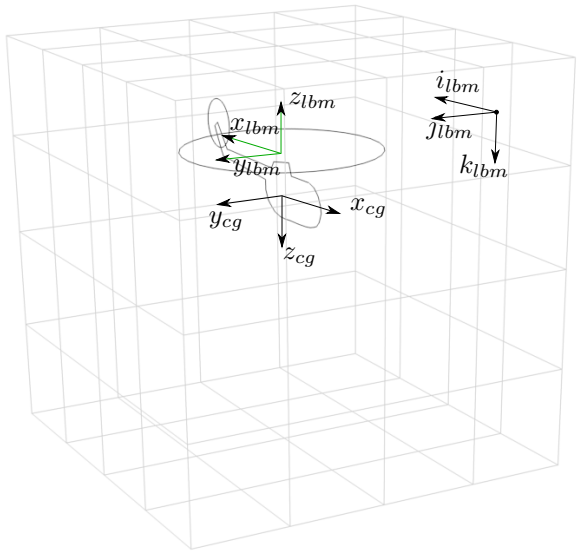

Figure 3: **Fluid domain with a grid of $N = 4$, coordinate system of the center of gravity, cg and coordinate system and grid indices of the LBM solver, lbm. For simplicity cell edges inside the domain are not shown. Adapted from [8].**

as the number of cells per edge length of the cubic domain. This resulted in a cell length $d = \frac{4R}{N}$. For the MBB Bo 105 helicopter with $R = 4.92\,\mathrm{m}$ the cell lenghts are listed in Ref. [8].

Because of the grid being fixed to the helicopter's center of gravity, it was moved according to the rotorcraft. In order to account for the movement, an Eulerian-Lagrangian approach as described by Meldi [13] was used. The rotorcraft's fuselage was modeled by wall boundary conditions equal to other objects in the flow field, as described by Friedmann [8]. Furthermore, the outer cells of the domain which were not used to model objects by wall boundary conditions, had to express a farfield boundary. To achieve this, impedance based boundary conditions were used, as described by Schlaffer [14]. In order to keep the solver stable when using the impedance boundary conditions, a Smagorinsky turbulence model with a Smagorinksy constant of $c_s = 0.075$ was used in all current simulations.

In contrast to the fully articulated rotor in the BEM, the rotor in the LBM was represented by one stationary layer of cells representing an actuator disk. This disk approximates a rotor with an infinite number of blades and imposes a force at every radial and circumferential position. As the range of r/R of the blade elements in the BEM was $0.233 \ldots 1$, the area of the rotor was formed by the rotor disk area minus a circle with $0.223R$ radius in the center. As the Cartesian grid was not able to adequately represent this rotor due to the low resolution which leads to large cell sizes, all cells that were not included completely inside the rotor had to be treated in a special way. As the grid was aligned with the rotor, the projection of the cells onto the rotor disk were squares. By intersecting the corresponding cells with a polygon representation of the rotor, the fraction of the cell that lay within the rotor was calculated. To identify the cells that were not fully within the disk, two circles with $R_i = R - 0.5\sqrt{2}d$ and $R_o = R + 0.5\sqrt{2}d$, concentric with the rotor disk were used. All cells, whose center point lay between these two circles, did not lie fully within the rotor, and had to be intersected with the disk. To reduce the computational cost, the implemented algorithm calculated the azimuth position of the cell's vertex and formed a circular segment using the angle $\Delta\Psi$ as it is shown schematically in green in Fig. 4.

$$\Delta\Psi = tan^{-1}\left(\frac{\sqrt{2}d}{R}\right) \tag{1}$$

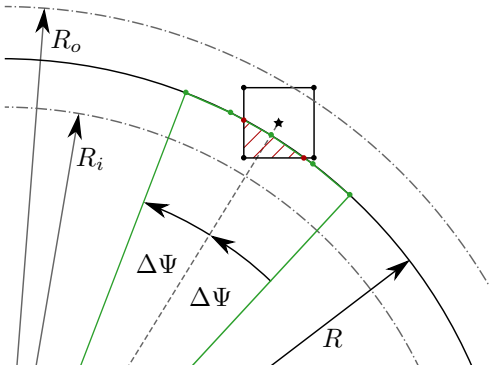

Figure 4: **Schematic view of the intersection of a cell with a convex six-sided polygon (green) representing a segment of the circular disk. Intersection-points and -area in red.**

This polygon was intersected with the cell using the linear algorithm of O'Rourke [15]. The area of the resulting polygon was calculated by the Shoelace formula [16], and a volume force proportional to the area inside the circular disk was imposed on the cell:

$$\boldsymbol{f} = \frac{A_{int}}{A_{Cell}} \boldsymbol{f_{perCell}} \tag{2}$$

where $\boldsymbol{f}$ is the volume force, A_{int} the area of the intersection, A_{Cell} the area of the cell and $\boldsymbol{f_{perCell}}$ the force acting per cell. To induce the force in the LBM, the scheme of Guo [17] was used. Due to the approximation of the circular disk as convex polygon, the resulting area of all cells within the rotor and

the polygons defined by the intersection, has to be smaller than the area of the circular disk. In order to be able to intersect cells with various radii, the number of edges that approximate the arc of the circular segment was adapted. Figure 5 shows the convergent behavior of the calculated area when increasing the number of segments that form the arc. In the further 40 segments were used, as it yielded satisfying accuracy. The circle with $0.223R$ in the center that is not included in the rotor was intersected with the grid in the same manner.

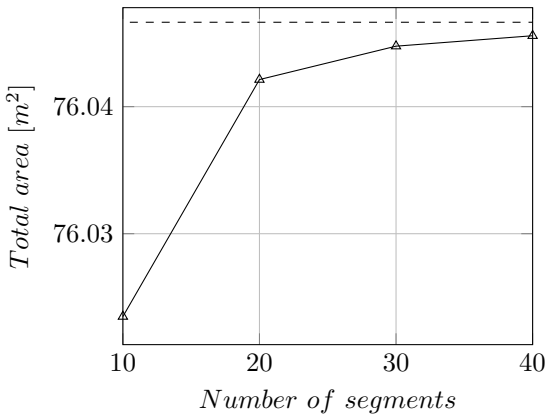

Figure 5: **Total area of circular rotor disk with $R = 4.92\,m$ calculated with polygon intersection from a grid with $N = 32$ using different numbers of segments (—△—). Analytic area as reference (- - -).**

2.3 Coupling via dynamic inflow and rotor thrust

As already mentioned the BEM and LBM were coupled using the inflow into the rotors and the rotor thrust. Instead of calculating the inflow from the aerodynamic forces using the Pitt-Peters inflow model, the forces were passed to the LBM simulation. After updating the boundary conditions the forces were imposed on the actuator disk and the LBM was advanced one step forward in time. Thereafter, the resulting velocities inside the actuator disk were passed to the BEM, which calculated the resulting blade motion and forces and advanced forward in time. As the actuator disk was located stationary in the computational domain of the fluid solver, the inflow velocities had to be transformed into the local coordinate system of the blade in the BEM and the thrust had to be transformed into the body fixed main rotor system of the BEM in order to be imposed on the actuator disk in the LBM.

Linear inflow and harmonic thrust (lin/harm)

The first model in this paper, denoted as lin/harm model, consisted of an approximation which calculated three states to describe each component of the inflow velocity and ten states to describe each component of the thrust. The inflow velocities were represented by a mean, sine and cosine coefficient:

$$\boldsymbol{u}(r,\Psi) = \boldsymbol{u_0} + \boldsymbol{u_s}\frac{r}{R}sin(\Psi) + \boldsymbol{u_c}\frac{r}{R}cos(\Psi) \tag{3}$$

with $\boldsymbol{u}$ being the velocity vector, Ψ being the azimuth angle, and subscript $0, s, c$ indicating the mean, sine, and cosine coefficients. The coefficients were calculated using the following integrals over all cells that lay fully within the rotor.

(4)

$$\boldsymbol{u_0} = \frac{1}{\pi}\iint \boldsymbol{u}dA \approx \frac{1}{N_{in}}\sum_{i=1}^{N_{in}}\boldsymbol{u_i}$$

$$\boldsymbol{u_s} = \frac{4}{\pi}\iint \boldsymbol{u}\frac{r}{R}sin(\Psi)dA \approx \frac{4}{N_{in}}\sum_{i=1}^{N_{in}}\boldsymbol{u_i}\frac{r}{R}sin(\Psi)$$

$$\boldsymbol{u_c} = \frac{4}{\pi}\iint \boldsymbol{u}\frac{r}{R}cos(\Psi)dA \approx \frac{4}{N_{in}}\sum_{i=1}^{N_{in}}\boldsymbol{u_i}\frac{r}{R}cos(\Psi)$$

With N_{in} being the number of cells that lay fully inside the rotor. This inflow description is equivalent to the representation in the Pitt-Peters model, which allows a direct comparison. The aerodynamic forces were transformed into the body-fixed rotorhub coordinate system (denoted by the index *lbm* in Fig. 3) and a harmonic analysis was performed. The thrust vector was represented as a sum of harmonic coefficients up to $N_{harm} = 10$.

$$\boldsymbol{T}(\Psi) = \sum_{l=0}^{N_{harm}}\Big(\boldsymbol{cos_l}(l\Psi) + \boldsymbol{sin_l}(l\Psi)\Big) \tag{5}$$

The zeroth cosine coefficient cos_0 represented the mean trust. The coefficients were calculated by multiplying the thrust $\boldsymbol{T_i}$ of the blade i with sine and cosine of a multiple of the azimuth angle Ψ:

$$\boldsymbol{cos_l} = \frac{2}{N_\psi}\sum_{i=1}^{N_b}\sum_{j=1}^{N_\psi}\boldsymbol{T_i}(\Psi_j)cos(l\Psi_j) \tag{6}$$

$$\boldsymbol{sin_l} = \frac{2}{N_\psi}\sum_{i=1}^{N_b}\sum_{j=1}^{N_\psi}\boldsymbol{T_i}(\Psi_j)sin(l\Psi_j)$$

where N_b is the number of blades. Using this representation of the thrust, the radial variation was neglected and the thrust was distributed evenly in radial direction. Although, this is a severe simplification, the fuselage was deflecting the downwash of the rotor outwards, which partially compensated the neglection of

©2016

the radial distribution of the thrust. Figure 6 shows the imposed thrust in z-direction in each cell over the radial coordinate of the blade at azimuth $\Psi = 90\,\text{deg}$ in hover. At the inner and outer boundary of the rotor disk, the polygon intersection of the rotor with the grid, which is described by Eqn. 2, reduced the imposed thrust. Furthermore, the z-component of the linearized velocity, wich was sent to the BEM after the linearization is shown. For comparison the positions of the blade elements in the BEM are included.

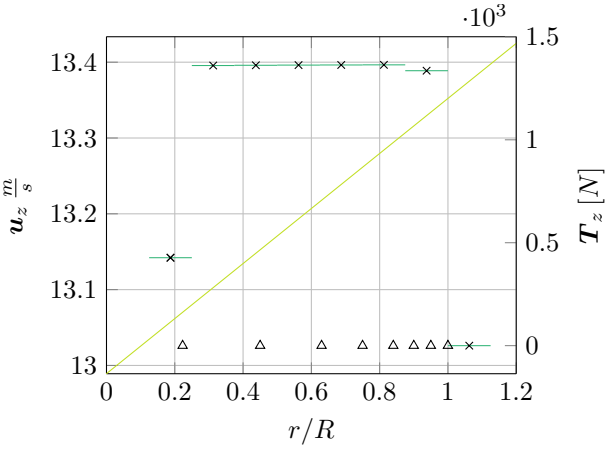

Figure 6: **Values of velocity(——) sent to the BEM and thrust(——) imposed in the LBM over the radial coordinate using the lin/harm model in hover at $\Psi = 90\,\text{deg}$. Positions of blade elements in BEM marked by (△), cell vertices marked by (×)**

Local inflow and local thrust (loc/loc)

The second model, denoted as loc/loc model, used the local values of the velocity in each cell to calculate the total velocity of the blade element relative to the air. Therefore, all cells within the rotor disk were passed to the BEM. For each blade element, the velocity of the nearest cell was imposed as inflow velocity. After superimposing the velocities resulting from the blade motion, the aerodynamic forces in all blade elements at all circumferential positions were calculated and sent to the LBM. An example of the resulting distribution of the velocity and thrust in hover is shown in Fig. 7 for an azimuth position of $\Psi = 90\,\text{deg}$. For convenience the positions of the blade elements in the BEM are included. As for the lin/harm model, the polygon intersection of the rotor with the grid reduces the imposed thrust in cells intersecting with the boundary of the rotor.

After receiving the local forces at all circumferential points and blade elements from the BEM, the value of the blade element nearest to the center of each cell was selected to be imposed as volume force on the fluid. As this selection process did not conserve the total thrust, the thrust in all cells was scaled by a factor. This factor resulted from the mean of each component of the force that was calculated in the BEM, divided by the sum of the component of the force imposed in all cells that lay inside or intersected with the rotor. By this measure, it was ensured that the BEM and LBM used the same thrust values.

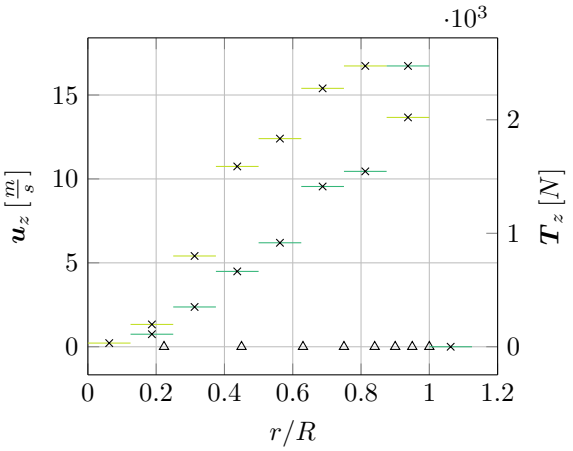

Figure 7: **Cell values of velocity(——) and thrust(——) of the loc/loc model over the radial coordinate in hover at $\Psi = 90\,\text{deg}$. Positions of blade elements in BEM marked by (△), cell vertices marked by (×)**

Calculation of trimmed state

Independent of the used model to describe inflow and thrust, the model was trimmed using a trim calculated by the Pitt-Peters model as initial value. To ensure that the flow field was fully developed, the LBM was given 1000 time steps with the calculated thrust. At the resolution of $N = 32$ this corresponded to $2.78s$. With a downwash velocity of approximately $11\frac{m}{s}$ this ensured that the free stream reached the far-field boundary, even if at $z_{lbm} = -3R$ a wall boundary deflected the stream.

Thereafter, the model was trimmed using the coupled LBM/BEM with the flow field from the previous trim as initial condition. As it had to be ensured that the fluid solution was stationary, the LBM was advanced for 1000 time steps in each trim step following the same procedure as previously discussed. A trim was found if the longitudinal and lateral residuals of the forces were below 50 N, the vertical below 100 N, the residual of the rolling moment below 50 Nm, and the residuals of pitching and yawing moments below 100 Nm. This algorithm is similar to the one used in Ref. [3].
Throughout this article, the tail rotor of the Bo 105

©2016

was not modeled using the coupled approach. Due to its small size, it would have been resolved by only four cells at a resolution of $N = 32$. Instead, the inflow to the tail rotor was calculated using the Pitt-Peters model. Nevertheless, as both rotors are inside the same computational domain, the model is, in principle, able to capture rotor-rotor interaction when both rotors are sufficiently resolved.

3 RESULT AND DISCUSSION

In order for the presented two-way coupled models to be valid, they have to be able to correctly depict the rotorcraft's flight dynamics even when arbitrary objects influence the flow field around the helicopter. Furthermore, they must show convergent behavior if the resolutions of the LBM and BEM are increased. As a first step, the behavior in stationary forward flight and in ground effect was assessed. Furthermore, the dynamic response of the models is compared to the Pitt-Peters reference model.

3.1 Stationary forward flight and influence of ground effect

In trimmed forward flight out of ground effect, both presented models showed good agreement concerning the required power which is shown in Fig. 8. For the lin/harm model the induced power is calculated from the mean thrust in z-direction, $\bar{T}_z$, and the mean induced velocity in z-direction, $\bar{v}_z$, of all cells that are fully inside the rotor. For the loc/loc model the induced power was calculated by summing the local thrust times the induced velocity over all cells that lay within or intersected with the rotor. Both models showed good agreement with the reference model concerning the induced power.

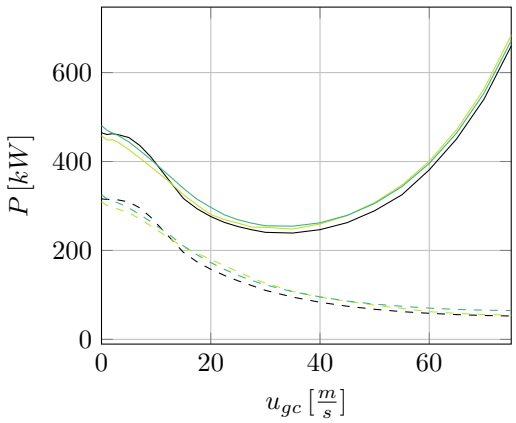

Figure 8: **Required power (——) and induced power(- - -) of the lin/harm (——), loc/loc (——), and Pitt-Peters model (——)**

Concerning the necessary inputs for the trimmed forward flight states, shown in Fig. 9, both presented models showed good agreement with the reference model concerning the collective and pedal input. In contrast to the power at forward speeds below 20 $\frac{\mathrm{m}}{\mathrm{s}}$, both presented models showed deviations from the reference model in the longitudinal and lateral input. At speeds above 20 $\frac{\mathrm{m}}{\mathrm{s}}$ the inputs of the presented and the reference model converged, although, the difference in the lateral input between the presented models and the reference did not fall below 5%.

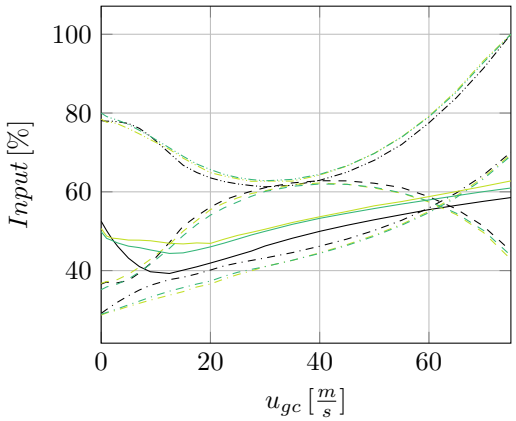

Figure 9: **Collective(-·-·-), pedal(- - -), lateral(——), and longitudinal input(-·-·-) of the lin/harm (——), loc/loc (——), and Pitt-Peters model (——) in trimmed forward flight**

When hovering in heights of $z < 3R$ the ground influences the rotor thrust at a given power [9,12]. This is equal to a reduction in the induced power at a given thrust [12, 18]. Among others, Cheeseman and Bennett [19] or Johnson [9] proposed models to account for the power reduction while hovering in ground effect. Neglecting blade loading effects, the Cheeseman model reduces to:

$$\frac{P_{IGE}}{P_{OGE}}|_{T=const} = 1 - \frac{1}{16}\frac{R^2}{z} \tag{7}$$

The model of Johnson describes the power reduction with use of an exponential function:

$$\frac{P_{IGE}}{P_{OGE}}|_{T=const} = \frac{1}{1 + e^{-2z/R}} \tag{8}$$

In order to calculate the power reduction in ground effect for the presented models, P_{OGE} and P_{IGE} in trimmed hover were extracted for various heights above ground. For $z > 3R$, $P_{OGE} = 480.9\,\mathrm{kW}$ and $P_{OGE} = 458.0\,\mathrm{kW}$ were obtained for the lin/harm and loc/loc model, which correlated well to the $P_{OGE} = 464.7\,\mathrm{kW}$ obtained using the dynamic inflow model of Pitt and Peters. The same was true for the

©2016

control inputs as can be seen in Fig. 9. The power required to hover in ground effect above a flat ground plane, perpendicular to the rotor's z-axis, is shown in Fig. 10.

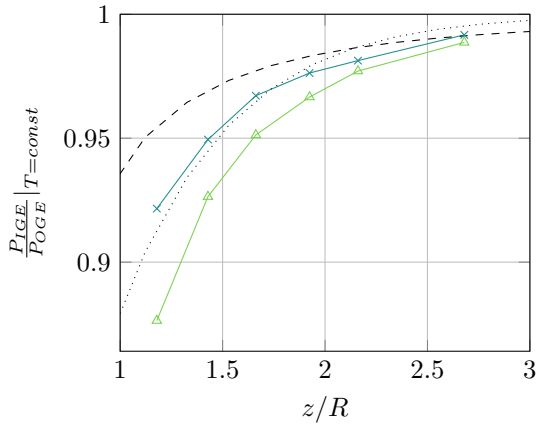

Figure 10: **Required power to hover in ground effect compared to power out of ground effect at constant thrust. Models of Cheeseman and Benett (- - -), Johnson (·····), the presented lin/harm model (—×—), and the presented loc/loc model (—△—)**

Both presented models showed a power reduction when hovering in ground effect. The lin/harm model showed less power reduction than the loc/loc model and was in good agreement with the model of Johnson. The loc/loc model showed an almost constant offset to the model of Johnson. This may result from the higher velocity of the rotor downwash which resulted from the thrust distribution of the blade. As the outer section produces the main part of the thrust and the loc/loc model did not use a linearisation, the velocities in the outer region of the downwash were higher, yielding different wake contraction ratios which influence the supportive effect on the rotor. Neither of the presented models was trimmable at heights below $z/R = 1.17894$, because vorticies formed below the fuselage which caused the used trim algorithm to diverge.

When flying forward in ground effect, the influence of the ground depends strongly on the interaction of the rotor wake with the ground. As the wake is swept rearward with the velocity of the rotorcraft, the supporting effect of the ground is diminishing fast [20]. The interaction of wake and ground resulted in a reduction of the required power compared to the flight out of ground effect, as it can be seen in Fig. 11.

When compared with the corresponding data from Ref. [12, 20], a similar behavior was observed, as the reduction in the required power became smaller with

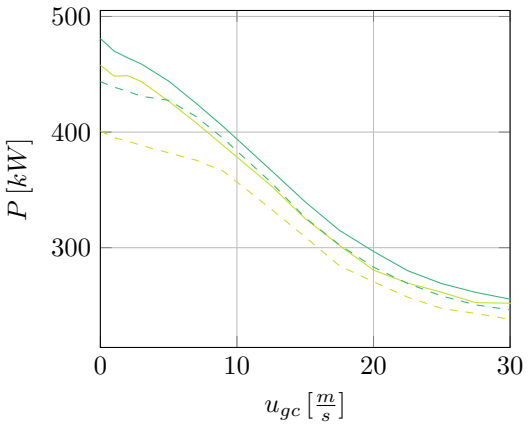

Figure 11: **Required power out(——) and in(- - -) ground effect of the lin/harm (——) and loc/loc (——) model at $z/R = 1.17894$.**

increasing forward speed. Nevertheless, the presented models did not show any increase of the required power at forward speeds approximately half the induced velocity. Furthermore, the power did not show a tendency to converge to the power out of ground effect at higher forward speeds. This may be caused by the limited resolution of the fluid simulation, which inhibited the formation of vortices and recirculation areas as they are described by [12]. Additionally, the actuator disk assumption yields a strongly simplified rotor wake. This may be oversimplified to approximate the extremely complicated flow field in this state [20].

3.2 Dynamic response to control inputs

In order to compare the flight dynamics of the two-way coupled models to the Pitt-Peters reference model, the rotorcraft motion resulting from step inputs was investigated. In order to substantiate that the usage of the steady state rotor as described in Sec.2.1 had no significant influence, the rotorcraft motion was compared to a simulation without this assumption while still using an actuator disk as representation of the rotor to model the inflow. In this simulation, every blade moved according to its own trajectory resulting from the equilibrium of external and inertial forces. The Pitt-Peters inflow model was used to calculate the inflow velocities for this comparison.

First, the response to a step input in the longitudinal cyclic with an amplitude 5% of the available range at $t = 1s$ was investigated. The required power, shown in Fig. 12, coincided with the power when using the steady state assumption. The same held for the rotorcraft motion, shown in Fig. 14, which showed slight deviations to the steady state rotor. Nevertheless, the reaction of the rotorcraft was captured adequately. As

©2016

a consequence, the simplification of a steady state rotor was considered to be valid for the given flight condition.

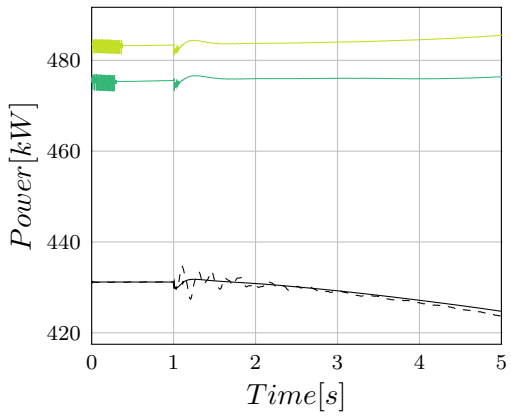

Figure 12: **Required power due to a step input in the longitudinal control in trimmed hover. Amplitude of the step input 5% of the available input range at $t = 1s$. Pitt-Peters model with steady state rotor (——) and full blade trajectory (- - -). Lin/harm(——) and loc/loc(——) model using $N = 32$.**

Concerning the required power of the rotorcraft shown in Fig. 12, both presented models overpredicted the power consumption in trimmed hover. When analyzing the rotorcraft motion in hover, shown in Fig. 14, a behavior similar to the reference model was observed for the velocities u_{cg}, and w_{cg} and the rotation rates p_{cg}, q_{cg}. The yawing rate r_{cg} showed significant deviations from the reference model starting at $t \approx 3\,\mathrm{s}$ and it did not follow the trends of the reference model. The velocity v_{cg} showed an opposite tendency when compared to the reference model which resulted in a wrong position. However, the remaining attitudes and positions were found to be in good agreement with the reference model.

As the second test case, the rotorcraft was trimmed at a forward velocity of $u_{cg} = 30\,\frac{\mathrm{m}}{\mathrm{s}}$ and a step input in the collective of 5% of the available input range was imposed at $t = 1s$. The required power is shown in Fig. 13. In order to show the validity of assuming a steady state rotor in the given flight condition, the required power was compared to the simulation when using full blade trajectories. After the step input, the required power was subject to fading oscillations when the blade trajectory was taken into account. As the step input in the collective caused all blades to flap with high amplitudes, lift and drag varied and caused these oscillations in the power required. When using the steady state rotor, the excessive flapping of the blades was not present and, therefore, there were no oscillations in the required power in this case. However, the mean power during the oscillations was equal to the power predicted by the steady state rotor simulation. After approximately $3s$ the damping of the blades due to the aerodynamic and centrifugal forces has eliminated the oscillations. Despite the different power requirements without it, the steady state assumption was supported by the rotorcraft motion. The rotorcraft's response was independent of the use of steady state rotors as can be seen in Fig. 15. Therefore, the assumption of steady state rotors was considered valid when analyzing the rotorcraft motion in the current operating conditions.

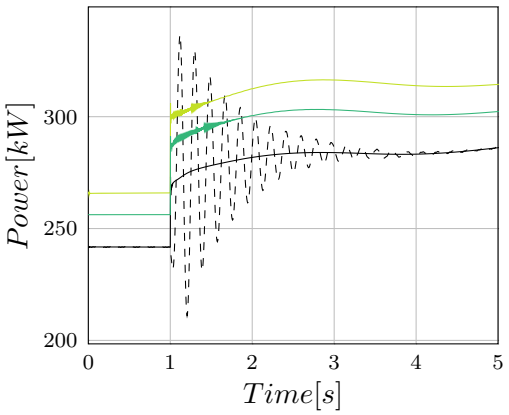

Figure 13: **Required power due to a step input in the collective control in trimmed forward flight at $u = 30\frac{m}{s}$. Amplitude of the step input 5% of the available input range at $t = 1s$. Pitt-Peters model with steady state rotor (——) and full blade trajectory (- - -). Lin/harm(——) and loc/loc(——) model using $N = 32$.**

Concerning the rotorcraft motion, the velocities u_{cg}, v_{cg} and w_{cg}, and the rates p_{cg}, q_{cg}, and r_{cg} showed good agreement with the reference model. Although the amplitudes of the presented models were underestimated when compared to the reference model, they showed good qualitative agreement, as all velocities and rates show the same trends as the reference model.

©2016

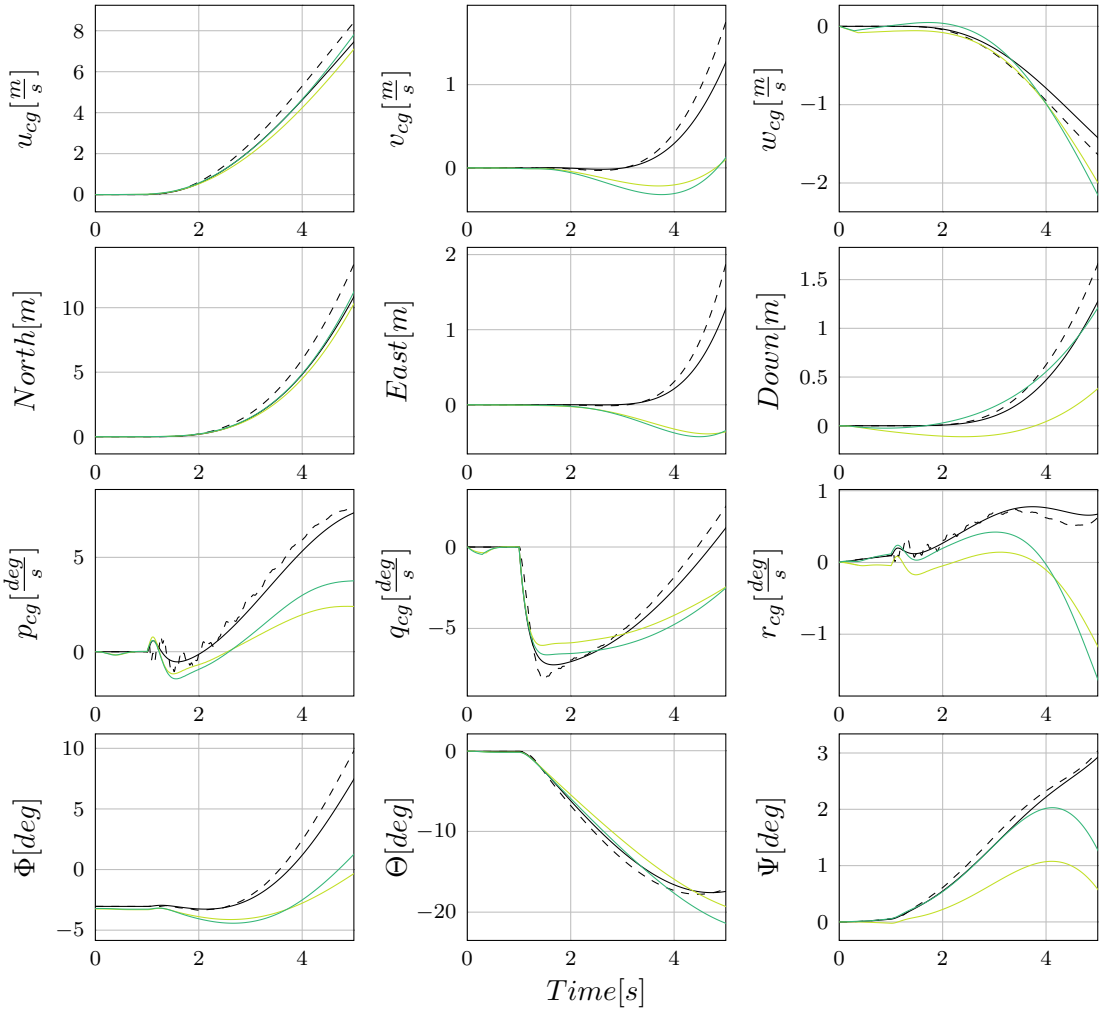

Figure 14: **Rotorcraft motion due to a step input in the longitudinal control in trimmed hover. Amplitude of the step input 5% of the available input range at $t = 1s$. Pitt-Peters model with steady state rotor (——) and full blade trajectory (- - -). Lin/harm (——) and loc/loc (——) model using $N = 32$.**

©2016

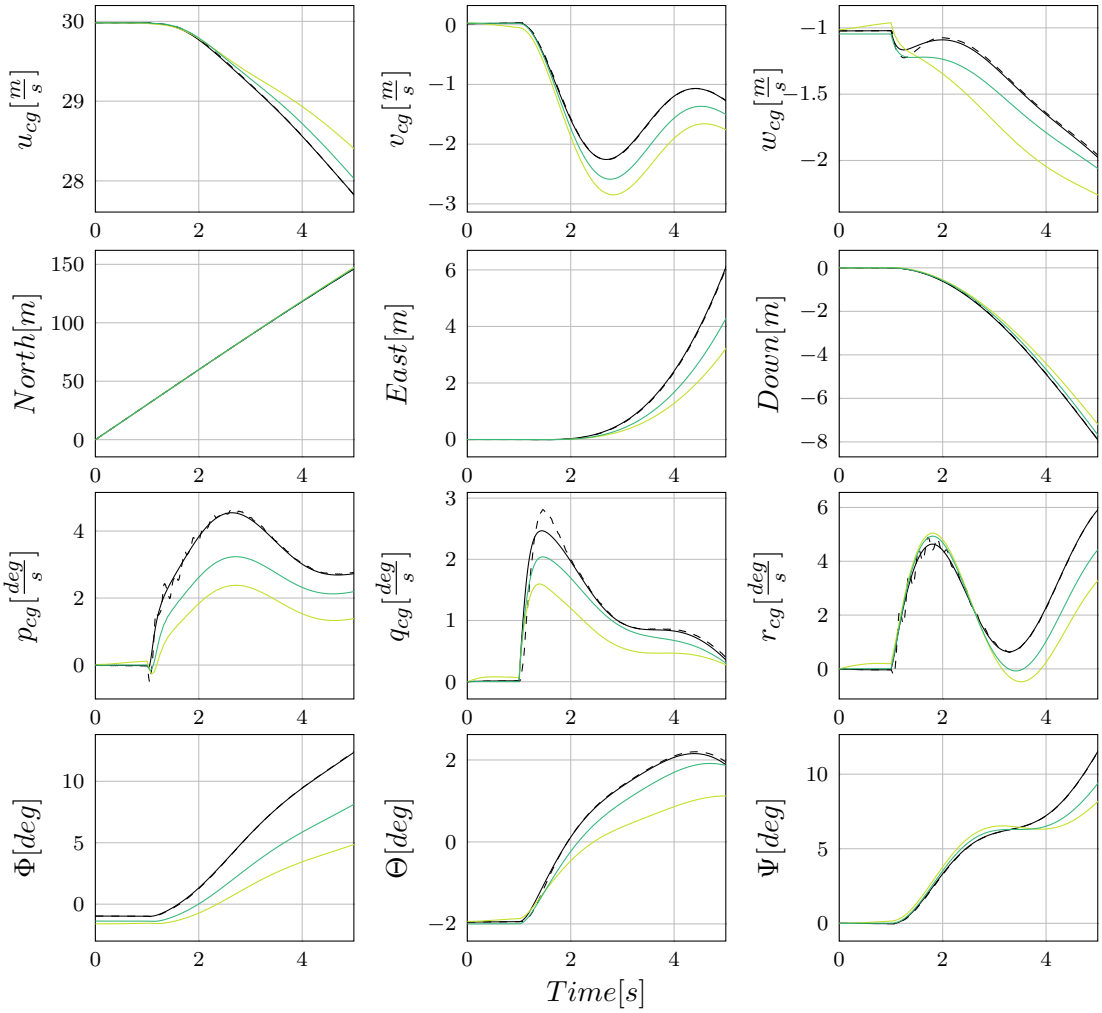

Figure 15: **Rotorcraft motion due to a step input in the collective control in trimmed forward flight at $u = 30\frac{m}{s}$. Amplitude of the step input 5% of the available input range at $t = 1s$. Pitt-Peters model with steady state rotor (——) and full blade trajectory (- - -). Lin/harm (——) and loc/loc(——) model using $N = 32$.**

4 CONCLUSIONS AND OUTLOOK

The ability of the presented real-time capable, two-way coupled fluid dynamics/flight dynamics models to correctly predict the influence of a ground plane on the rotorcraft's power in hover was investigated. The results correlated well in power and controls for stationary forward flight and predicted the ground effect in both hover and forward flight. The dynamic reactions to step inputs in trimmed flight were found to be in good agreement with the reference model. This was the first step to validate and enhance the models to be used for piloted simulations in pilot training facilities. Nevertheless, convergence behavior needs to be investigated along with detailed validation of the resulting dynamic inflow.

The shown results were obtained in real-time using a Nvidia GeForce 980 Ti for the flow computations by the LBM solver. As the time required by the LBM solver dominated the computational time necessary for one time step, doubling the resolution while preserving the real-time capability will require roughly 2^4 times the computational power. Nevertheless, increasing the spatial resolution is indispensable in order to be able to couple the tail rotor in the same manner as it was done for the main rotor to include rotor-rotor interaction phenomena. Furthermore, the LBM solver's ability to capture the influence of the fuselage and surrounding objects will be enhanced as finer approximations of the geometries are possible. Because a single graphics card is not able to provide the required computational power, efficient, distributed computation strategies will be explored. An increased resolution will also permit to use individual blades in the LBM instead of an actuator disk. These measures are expected to enhance the dynamics of the BEM and allow better representations of the rotor wake.

References

[1] Pitt, D. M., and Peters, D. A. Theoretical predictions of dynamic-inflow derivatives. *Vertica 5* (1981), 21–34.

[2] Gennaretti, M., Gori, R., Cardito, F., Serafini, J., and Bernadini, G. A space-time accurate finite-state inflow model for aeroelastic applications. *72nd Annual Forum of the American Helicopter Society* (2016).

[3] Oruc, I., Horn, J. F., Polsky, S., Shipman, J., and Erwin, J. Coupled flight dynamics and cfd simulations of the helicopter/ship dynamic interface. *71st Annual Forum of the American Helicopter Society* (2015).

[4] Polsky, S., Wilinson, C. H., Nichols, J., Ayers, D., Mercado-Perez, J., and Davis, T. S. Development and application of the safedi tool for virtual dynamic interface ship airwake analysis. *AIAA SciTech* (2016).

[5] Amsallem, D., Cortial, J., and Farhat, C. Towards real-time cfd-based aeroelastic computations using a database of reduced-order information. *AIAA Journal Vol. 48* (2010).

[6] Owen, I., and Padfield, G. P. Integrating cfd and piloted simulation to quantify ship-helicopter operating limits. *Aeronautical Journal* (2006).

[7] Rubenstein, G., Moy, D. M., Sridharan, A., and Chopra, I. A python-based framework for real-time simulation using comprehensive analysis. *72nd Annual Forum of the American Helicopter Society* (2016).

[8] Friedmann, L., Ohmer, P., and Hajek, M. Real-time simulation of rotorcraft downwash in proximity of complex obstacles using grid-based approaches. *70th Annual Forum of the American Helicopter Society* (2014).

[9] Johnson, W. *Helicopter Theory*, 2nd ed. Dover Publications, New York, 1994.

[10] Hänel, D. *Molekulare Gasdynamik*, 1st ed. Springer-Verlag, Berlin Heidelberg, 2004.

[11] Wolf-Gladrow, D. A. *Lattice-Gas Cellular Automata and Lattice Boltzmann Models - An Introduction*, 1st ed. Springer-Verlag, Berlin Heidelberg, 2005.

[12] Leishman, J. *Principles of Helicopter Aerodynamics*, 2nd ed. Cambridge University Press, New York, 2008.

[13] Meldi, M., Vergnault, E., and Sagaut, P. An arbitrary lagrangian-eulerian approach for the simulation of immersed moving solids with lattice boltzmann method. *Journal of Computational Physics 235* (2013), 182–198.

[14] Schlaffer, M. *Non-Reflecting Boundary Conditions for the Lattice Boltzmann Method*. PhD thesis, Technical University of Munich, 2013.

[15] O'Rourke, J., Chien, C.-B., Olson, T., and Naddor, D. A new linear algorithm for intersecting convex polygons. *Computer Graphics and Image Processing 19* (1982), 384–391.

[16] Braden, V. The surveyor's area formula. *The College Mathematics Journal 17* (1986).

[17] Guo, Z., Zheng, C., and Shi, B. Discrete lattice effects on he forcing term in the lattice boltzmann method. *Physical Review E 65* (1973).

©2016

[18] Khromov, V., and Rand, O. Ground effect modeling for rotary-wing simulation. *26th International Congress of the Aeronautical Sciences* (2008).

[19] Cheeseman, I., and Bennett, W. The effect of the ground on a helicopter rotor in forward flight. *ARC R&M 3021* (1955).

[20] Chen, R. T. N. A survey of nonuniform inflow models for rotorcraft flight dynamics and control applications. *15th European Rotorcraft Forum* (1989).

©2016